Final Technical Report for USGS Award G11AP20055

Fully Nonlinear Modeling of Strong Ground Motion From M7.0 Earthquakes on the Salt Lake City Segment of the Wasatch Fault, Utah: Request for Supplemental Funding

February 1, 2011 - January 31, 2013

Principal Investigator:*

Kim B. Olsen
Dept of Geological Sciences, San Diego State University
5500 Campanile Dr, San Diego, CA 92182-1020
ph 619 594 2649, fax 619 594 4372
email kbolsen@sciences.sdsu.edu

* D. Roten also contributed significantly to the work reported here.

Abstract

The current project is a continuation of the research carried out with funding from NEHRP USGS Awards 06HQGR0205 and 06HQGR0206. This previous research predicted broadband (BB, 0-10Hz) ground motions in the Salt Lake Basin (SLB) during M 7 earthquakes on the Salt Lake City (SLC) segment of the Wasatch fault (WFSLC). Average horizontal spectral accelerations (SAs) at 5 and 10 Hz (0.2s-SAs and 0.1s-SAs, respectively) calculated from the (linear) BB synthetics exceeded estimates from four recent ground motion prediction equations (GMPEs) at near-fault (< 5 km) locations on the sediment generally by more than one standard deviation. The overprediction of the near-fault GMPE values was largely eliminated after accounting for near-surface soil nonlinearity with 1D simulations along E-W profiles in the Salt Lake basin, reducing the SAs from the simulations by up to 70%. The nonlinear simulations along the E-W profiles used a simple soil model based in part on published laboratory experiments on Bonneville clay samples.

Here, we carry the nonlinear (NL) soil aspect of this work further by generating and applying average frequency-dependent correction functions for nonlinear soil effects in the SLB. Towards this goal, we analyzed NL SAs as a function of the corresponding linear SAs for three different Quaternary site response units (SRUs). To calculate the corresponding linear SAs, we ran 1-D simulations with the same input signal and the same velocity profile as in the nonlinear simulations, but define the material inside the entire soil column as linear. We considered 454 sites and a total of 21,792 1-D simulations to analyse the relations between linear and nonlinear SAs, from which we establish amplitude-dependent relations betweens SAs. Coefficients for these relations are calibrated for each considered frequency and each of the three site response units, and we apply these relations to correct our BB SA maps for nonlinear soil behavior. We find that, after taking soil nonlinearity into account, the largest 1s-SAs still occur on the hanging wall side of the fault, where they exceed 0.75 g. 0.2s-SAs are generally above 1 g within a few km of the fault on the hanging-wall and on the footwall sediments in the central SLB. In a few isolated areas, 0.2s-SAs exceed 1.25 g, especially on Q02 in the southern part of the SLB. Near-fault PGAs range from 0.45 to >0.6g.

Compared to ground motion maps generated in previous studies (Wong *et al.*, 2002b; Solomon *et al.*, 2004), our ground motion values are lower and have a different spatial pattern. The differences between our ground motion results and those obtained by Wong *et al.* (2002b) and Solomon *et al.* (2004) are likely caused by differences in the simulation methods. 0.2s-SAs and 0.1s-SAs corrected for nonlinear soil behavior compare favorably with values predicted by four GMPEs, including areas at close distances (< 5 km) from the rupture. However, on our maps the ground motions decrease more rapidly with distance from the surface rupture. Further comparisons against strong motion data are required to validate the simulated ground motions in the future.

Bibliography of all publications resulting from the work performed under the award

Roten, D., Olsen, K.B., and Pechmann, J.C. (2012). 3-D Simulations of M 7 Earthquakes on the Wasatch fault, Utah, Part II: Broadband (0-10 Hz) Ground Motions and Nonlinear Soil Behavior, *Bull. Seism. Soc. Am.* **102**, 2008-2030.

Final Technical Report

Introduction

The Wasatch fault in northern and central Utah is a major normal fault that separates the Salt Lake Basin to the west from the Wasatch Range to the east. The Salt Lake City segment of the Wasatch fault (WFSLC) represents the most obvious source of seismic hazard to the SLB, a major metropolitan area inhabited by more than a million people. Paleoseismological studies (Black *et al.*, 1995; McCalpin and Nishenko, 1996; McCalpin and Nelson, 2000) have shown that the WFSLC ruptures during large M$\sim$7 surface faulting earthquakes with an average return interval of 1350$\pm$200 years, and that the last such event occurred approximately 1230$\pm$60 years B.P. Based on these findings, McCalpin and Nelson (2000) have estimated the probability of an M$\sim$7 earthquake occurring during the next 100 years to be 16%; Wong *et al.* (2002a) have estimated that the probability for the next 50 years is 6 to 9%.

Worldwide there are few near-fault strong ground motion records from M$\geq$6 normal-faulting earthquakes, and no records for M$\geq$7 normal-faulting earthquakes (Chiou *et al.*, 2008; Campbell and Bozorgnia, 2008). As a result, there is a large uncertainty associated with the ground motions expected from future M 7 earthquakes on the WFSLC.

Adding to this uncertainty are the soft sediments of the SLB, which are more than 1km deep in some places. Such unconsolidated deposits may significantly amplify the seismic ground motion during large earthquakes, and contribute drastically to the loss of life and property, as has been demonstrated repeatedly during earthquakes elsewhere. Nonlinear soil behavior, on the other hand, may lead to a deamplification of strong ground motion, especially at higher frequencies (>1 Hz).

It is vital to gain a quantitative understanding of the ground motion expected from future large earthquakes on the WFSLC. Roten *et al.* (2011) and Roten *et al.* (2012) addressed this issue by performing 0-1 Hz 3D finite difference (FD) simulations of wave propagation in the SLB based on a detailed velocity model, a realistic fault geometry, and rupture models derived from spontaneous rupture simulations. The synthetic ground motions were then extended to 10 Hz by combining our low-frequency (0-1 Hz) synthetics with a high-frequency (1-10 Hz) component based on scattering theory. They also performed simulations of nonlinear soil response, which typically becomes important at higher frequencies, for sites on three cross-basin profiles.

Here, we carry the nonlinear (NL) soil aspect of this work further by generating and applying average frequency-dependent correction functions for nonlinear soil effects in the SLB. Towards this goal, we analyze NL SAs as a function of the corresponding linear SAs for different site response units. To calculate the corresponding linear SAs, we run 1-D simulations with the same input signal and the same velocity profile as in the nonlinear simulations, but defined the material inside the entire soil column as linear. We then analyse the relations between linear and nonlinear SAs, from which we establish amplitude-dependent relations betweens SAs. Coefficients for these relations are calibrated for each considered frequency and each of the three site response units, and we apply these relations to correct our BB SA maps for nonlinear soil behavior.

Background

3-D numerical simulations are routinely used to model the dynamic fault rupture process and the resulting seismic wave propagation in strongly heterogeneous media, providing a deter-

ministic characterization of the ground motions during scenario earthquakes (e.g. O'Connell *et al.*, 2007; Olsen *et al.*, 2009). However, these simulations are computationally expensive and therefore typically limited to maximum frequencies of ∼1 Hz. Recently, increases in the computational resources available to science has allowed to extend this limit to higher frequencies. Cui *et al.* (2010), for example, simulated an M_w8 earthquake on the southern San Andreas fault for frequencies up to 2.0 Hz using a minimum shear-wave velocity of 400 $m{\cdot}s^{-1}$. But even the fastest supercomputers available today cannot deterministically simulate ground motion for the whole 0-10 Hz frequency range that is relevant for engineering. For this reason BB methods have been developed which combine deterministic low-frequency (LF) ground motions with a high-frequency (HF) component to generate synthetic seismograms for the entire frequency range of engineering interest. A number of methods use stochastic seismograms to generate the HF component of the signal (e.g. Pitarka *et al.*, 2000; Mena *et al.*, 2006). Other methods incorporate the physics of wave scattering at frequencies above 1 Hz to simulate the HF ground motions (e.g. Zeng *et al.*, 1995; Hartzell *et al.*, 2005). Mai *et al.* (2010) combined HF (1-10 Hz) S-to-S back-scattering seismograms with LF (0-1 Hz) deterministic seismograms for the 1994 Northridge earthquake, and found that the resulting broadband synthetics were consistent with observations for the modeled frequency range. Mena *et al.* (2010) developed the method further by incorporating dynamically consistent source-time functions and accounting for finite-fault effects in the computation of the HF waveforms. Their method also includes corrections for local site effects that use frequency- and amplitude-dependent amplification functions (Borcherdt, 1994).

Deterministic 3-D LF simulations typically do not take soil nonlinearity into account, since this effect is not very important at frequencies below 1 Hz. For the HF component of the ground motion, however, non-linear soil behavior may become an important factor during strong earthquakes. 0–10 Hz simulations of wave propagation in nonlinear media are primarily limited to 1-D (e.g. Hartzell *et al.*, 2004) and 2-D (e.g. Bonilla *et al.*, 2006). In geotechnical engineering it is standard practice to apply an equivalent linear 1-D model (e.g. Schnabel *et al.*, 1972). It is well accepted that this physical model is limited to a certain strain level above which the soil behavior becomes very complex. In these cases a fully non-linear calculation needs to be performed in order to accurately estimate the soil response.

Wong *et al.* (2002a) and Solomon *et al.* (2004) who produced maps of average expected peak ground acceleration (PGA) and spectral acceleration at periods of 0.2s and 1s (0.2s-SAs and 1s-SAs, respectively) in and around the SLB for M7 scenario earthquakes on the WF-SLC. Their method was based on a combination of ground motion attenuation relationships and stochastic modeling. To account for site effects and nonlinear soil behavior, Wong *et al.* (2002a) and Solomon *et al.* (2004) defined five generalized site response units and calculated 1-D amplification factors for each unit as a function of input PGA and unconsolidated sediment thickness. Shear modulus reduction and hysteretic damping were incorporated using an equivalent-linear formulation (Silva *et al.*, 1998). The M 7 scenario earthquake ground motion maps by Wong *et al.* (2002a) and Solomon *et al.* (2004) show the highest PGAs and 0.2s-SAs near the surface break on the footwall side in the central SLB and on the hanging wall side in the southern part of the SLB. These areas are covered by stiff gravel and sand deposits, which amplify the ground motions at higher frequencies. Sites on the hanging-wall side of the fault that are underlain by soft lacustrine and alluvial silts, clays, and sands exhibit lower ground motions due to damping by nonlinear soil response. For a period of 1s, Wong *et al.* (2002a) and Solomon *et al.* (2004) predict the largest ground motions at near-fault sites on deep hanging-wall sediments in the southern SLB as well as on shallow footwall sediments in the central SLB (up to 1.3-1.5g).

Recently, Roten *et al.* (2012) predicted BB (0-10Hz) ground motions in the SLB during M 7 earthquakes on the SLC segment of the WFSLC (Fig. 1). Roten *et al.* (2012) generated BB synthetics using the BB method of Mai *et al.* (2010), where the generation of the HF part of the seismogram is based on multiple shear-to-shear (S-to-S) backscattering theory. The LF FD synthetics are combined with the HF scatterograms (maximum frequency 20 Hz) using a simultaneous amplitude- and phase-matching algorithm (Mai and Beroza, 2003). This approach finds the optimum matching frequency within a predefined frequency band and minimizes mismatches in both amplitude and phase. The matching frequency depends on the site and component. The matching frequency was between 0.8 and 1.0 Hz, and they applied the scattering operators to LF synthetics at every 5th node on the surface of the computation grid. This resulted in a spatial resolution of 200 m and a grid dimension of 225$\times$ 300 nodes (67,500 sites).

Figure 2 compares BB SAs as function of distance along two cross-sections with SAs predicted by four next-generation ground motion prediction equations (GMPEs): Boore and Atkinson (2008), Campbell and Bozorgnia (2008), Abrahamson and Silva (2008) and Chiou and Youngs (2008). In the remainder of this text, we will refer to these next-generation attenuation (NGA) relations as BA08, CB08, AS08 and CY08, respectively. For each site along the three cross-sections, Roten *et al.* (2012) used the 3-D fault model and 3-D velocity mesh to calculate the rupture distance R_{Rup}, the horizontal distance to both the top of the rupture, R_x, and to the surface projection of the rupture, R_{JB}, the average shear-wave velocity in the top 30 meters V_{S30}, and other site-specific parameters required by the GMPEs.

Figure 2 (left) shows BB 0.2s-SAs along cross-section P0 for rupture model B. The highest accelerations are encountered on the hanging-wall close to the fault, where the SAs predicted by all four GMPEs are exceeded for $R_x < 5$ km. The GMPE by BA08, which predicts the lowest amplitudes of the four considered relations, yields 0.2s-SAs that are two to four times lower than the BB 0.2s-SAs in this area. Even the relations of CY08 and AS08, which predict the highest amplitudes, are exceeded at near-fault hanging-wall locations. On the footwall side of the fault, the BB SAs are in good agreement with BA08. Beyond fault distances of more than 12 km on the hanging-wall side, however, the BB SAs quickly drop below the values predicted by all four NGA models. The simulated SAs are generally within one standard deviation of those predicted by the NGA relations everywhere along the cross-section.

Figure 2 (right) shows BB 0.2s-SAs along cross-section P1 for rupture model B'. This example includes the most extreme values produced by our simulations, as rupture model B' yields the largest ground motions of all six scenarios and the cross-section P1 runs through the area with the largest linear BB SAs for this scenario. For fault distances less than 9 km on the hanging-wall side, the linear BB SAs exceed the predictions of all four considered NGA models by more than one standard deviation. All four GMPEs predict the highest SAs on the footwall side of the fault, which is the opposite of the pattern produced by the BB simulations. Average horizontal spectral accelerations (SAs) at 5 and 10 Hz (0.2s-SAs and 0.1s-SAs, respectively) calculated from the (linear) BB synthetics exceeded estimates from four recent ground motion prediction equations (GMPEs) at near-fault (< 5 km) locations on the sediment generally by more than one standard deviation.

Figure 3 shows SAs predicted by the four NGA models for the same profiles as depicted in Figure 2, but compares them with spectral accelerations calculated from the fully nonlinear synthetics (NL SAs). For cross-section P0 and rupture model B (Fig. 3 left), the NL 0.2s-SAs are generally consistent with the values predicted by AS08 and CY08 at near-fault ($R_x < 10$ km) hanging-wall locations. Spectral accelerations predicted by BA08 and CB08, however, are up to 50% lower than NL 0.2s-SAs in the hanging wall. Compared to the BB 0.2s-SAs,

the NL 0.2s-SAs are reduced by up to 45%. On the footwall side and for $R_x > 15$ km on the hanging-wall side, the NL 0.2s-SAs are almost identical with BB 0.2s-SAs. This observation suggests that the input ground motion at these sites is not sufficient to trigger nonlinear soil response.

Roten *et al.* (2012) also calculated the site response at every point along the three profiles using the soil models that represent the upper and lower bound of soil nonlinearity, by taking $\gamma_r \mp \sigma$ as the reference strain and $\xi_{\max} \pm \sigma_r$ as maximum damping ratio. The hatched area in Figure 3 (left) indicates the range of NL 0.2s-SAs obtained from the upper and lower bound parameters. The choice of γ_r and $\xi_{\max}$ only affects the ground motion at sites where a significant deamplification due to soil nonlinearity takes place; that is, on the hanging wall site of the fault for R_x less than about 10 km. Using the lower bound soil model increases NL 0.2s-SAs by up to 30% at individual sites, while the upper bound model decreases them by up to 25% compared to the reference nonlinear model.

Figure 3 (right) makes the same comparison with NL 0.2s-SAs for cross-section P1 and rupture model B'. Compared to the linear case, 0.2s-NL SAs are reduced by up to 70%, with the largest reduction on the hanging-wall side within 10 km fault distance. The simulated 0.2s-SAs are in general agreement with the GMPEs. Even when the uncertainty associated with the nonlinear soil parameters is taken into account (hatched area in Fig. 3, right), the NL 0.2s-SAs remain mostly inside one standard deviation of the minimum and maximum of the four considered NGA predictions. The largest NL 0.2s-SAs along cross-section P1 occur close to the surface rupture on the footwall side, which is consistent with the pattern predicted by the four GMPEs. Along cross-section P1, all locations on the hanging-wall side belong to site response unit Q01 (Fig. 1), while the footwall side is located on unit Q03 and on rock. This fact suggests that the degree of nonlinearity is controlled by the local site response unit.

Nonlinear correction functions

From the NL simulations carried out along the three cross sections (see above), it is clear that nonlinear effects must be considered throughout the SLV for the M 7 WF scenarios in order to provide useful ground motion predictions for structural engineers. Here, we generate and apply average frequency-dependent correction factors for nonlinear soil effects in the SLB by analyzing NL SAs as a function of the corresponding linear SAs for the three different SRUs. To calculate the corresponding linear SAs, we ran 1-D simulations with the same input signal and the same velocity profile as in the nonlinear simulations, but defined the material inside the entire soil column as linear. We considered 454 sites located on soil along the three profiles (182 on Q01, 135 on Q02 and and 137 on Q03) and six different earthquake scenarios. For each site and each scenario, 8 1-D simulations were required: one for each horizontal component with four different soil models: mean nonlinear model, upper-and lower bound nonlinear models, and linear model. Therefore, a total of 21,792 1-D simulations were considered to analyse the relations between linear and nonlinear spectral accelerations.

Table 1 summarizes the properties of the different SRUs. Figure 4 (A) shows NL 0.2s-SAs as a function of linear 0.2s-SAs for all points located on SRU Q01. While the linear time series exhibit 0.2s-SAs up to 50 $\mathrm{m{\cdot}s^{-1}}$ ($\sim$5g), the NL ground motions do not exceed 27 $\mathrm{m{\cdot}s^{-1}}$. The linear SAs and NL SAs correlate strongly for small accelerations. The effect of hysteretic damping becomes appreciable for linear SAs above $\sim$5 $\mathrm{m{\cdot}s^{-2}}$, and the relation between linear and NL 0.2s-SAs resembles a sine-shaped curve. However, there is a large scatter in the linear-nonlinear SA data, even for relatively low levels (< 10 $\mathrm{m{\cdot}s^{-2}}$) of linear spectral acceleration.

The linear-nonlinear 0.2s-SAs comparison for SRU Q02 (Fig. 4 B) implies a more linear site response and less variability than for Q01. Sites located on Q03 (Fig. 4 C) exhibit an even smaller difference between nonlinear and linear 0.2s-SAs . Additionally, the linear ground motion on Q03 tends to be lower than on the other two SRUs, since Q03 is almost entirely located on the footwall side or at sites located more than 15 km from the surface rupture on the hanging wall side of the WF.

The comparisons between NL and linear 0.2s-SAs presented in Fig. 4 suggest that the degree of nonlinearity strongly depends on the local SRU, with the highest deamplification on Q01 and the most linear behavior on Q03. This result is somewhat surprising, as SRU Q01 was assigned the highest plasticity index (PI'=40), which implies a higher reference strain and, therefore, supposedly a more linear behavior (e.g. Vucetic and Dobry, 1991). However, there are other factors apart from the reference strain that influence the degree of nonlinearity: the total depth of the nonlinear layer (that is, the depth to the R_1 interface), and the average shear-wave velocity in the soil column.

Figure 5 (A) shows the distribution of the average shear wave velocity in the top 30 m, V_{S30}, for the three SRUs along the three cross-sections inside the computational domain. The V_{S30} values shown in the histograms were computed from the velocity mesh for the FD simulations, where a minimum v_s of 200 m·s−1 was imposed for computational reasons. V_{S30} is lower than 300 m·s^{-1} at most sites classified as Q01, while Q02 is characterized by a V_{S30} of 250 – 550 m·s^{-1}. Sites belonging to Q03 typically have a V_{S30} between 350 and 700 m·s^{-1}.

The backbone curve is scaled with the maximum shear stress τ_0 that the material can support in the initial state. τ_0 is proportional to the reference strain γ_r and the low-strain shear modulus

$$G_0 = \rho v_s^2. \tag{1}$$

Because G_0 is proportional to the square of the shear-wave velocity, v_s has a greater impact on the material strength than γ_r. This dependence is illustrated in Figure 6, which shows the theoretical strain-stress relationship according to Masing's rules for two specimens with $\gamma_r = 0.1\%$ and shear-wave velocities of 250 and 300 m·s^{-1}, respectively. Both materials are subjected to a cyclic shear stress up to ∼100 kPa. Figure 6 illustrates how the lower v_s results in a higher energy dissipation, which is proportional to the area of the hysteresis loop (Ishihara, 1996).

Figure 5 (B) shows the distribution of the depth to the R_1 interface for the three SRUs, which corresponds to the total thickness of the nonlinear layer. Like the V_{S30}, the depth to R_1 shows a different distribution on the three SRUs. On Q01, R_1 is deeper than 100 m for the majority of the sites, but it is often encountered at depths of less than 50 m on SRU Q03. Unit Q02 shows an intermediate distribution. A thinner nonlinear layer means that vertically propagating SH waves will encounter hysteretic damping on a smaller fraction of the path, and it is less likely that their amplitude will be reduced significantly by the time they reach the surface. The differences among the three SRUs in the distributions of R_1 depths and V_{S30} values explain why SRU Q03 exhibits the most linear behavior and the strongest nonlinear damping is encountered for SRU Q01, with an intermediate behavior for Q02.

The distribution of V_{S30} and the depth to R_1 along the three cross-sections is quite representative of the distribution on the entire computational domain (Fig. 5). We can use this observation to define nonlinear correction functions that depend on the SRU and the amplitude of linear spectral accelerations. To approximate the linear-nonlinear relationship (Fig. 4) a second-order polynomial was fit to the data after taking the natural logarithm:

$$\ln(\mathrm{SA_{NL}}) = a + b \cdot \ln(\mathrm{SA_{LN}}) + c \cdot \ln^2(\mathrm{SA_{LN}}) \tag{2}$$

where SA_{NL} represents the NL 0.2s-SAs and SA_{LN} the corresponding linear values. As we expect a strong correlation between linear and nonlinear values for low levels of SA_{LN}, we forced the offset a to zero in the least squares inversion. This constraint makes the function pass through (1,1) due to the logarithm in equation 2.

The solid line in Figure 4 (A) shows the nonlinear correction function that was fit to the data for Q01, for which we obtained b=1.17 and c=-0.13. We also determined the coefficients b and c for the linear-nonlinear corrections that were obtained from the upper- and lower-bound models of nonlinearity for Q01 (dashed lines in Fig. 4 A). The sensitivity of the NL spectral acceleration to the soil parameterization is significant: for linear 0.2s-SAs of 20 $m{\cdot}s^{-2}$, for example, the correction function predicts a NL 0.2s-SAs of 11 $m{\cdot}s^{-2}$, while the upper bound nonlinear model yields only $\sim$7 $m{\cdot}s^{-2}$; the lower bound model predicts 14 $m{\cdot}s^{-2}$. For SRU Q02 and 0.2s-SAs (Fig. 4 B) we obtain b=1.11 and c=-0.08 with the mean nonlinear model, which reflects the more linear behavior encountered on this SRU. For Q03, the polynomial function deviates only slightly from one, as the least-squares inversion yields b=1.06 and c=-0.05.

We determined the coefficients b and c for all of the frequencies considered and PGA. For PGV we allowed the coefficient a to vary, since the slope of the relation between nonlinear and linear PGVs deviates from one for linear PGVs below 1 $m{\cdot}s^{-1}$.

Ground motion maps corrected for nonlinearity

We now employ the site- and amplitude-dependent correction functions defined by equation 2 and correct the linear BB spectral acceleration maps (Fig. 7 from Roten *et al.* (2012)) for effects of nonlinear soil behavior. For each node on the $45{\times}60$ km^2 grid, the local SRU was determined using a digitized version of the McDonald and Ashland (2008) site response map (Fig. 1). Then we calculated the nonlinear SAs from the corresponding linear SAs using the coefficients b and c appropriate for the given SRU and frequency.

Figure 7 (left) and Figure 8 (left) show 0.2s-SAs for scenario B before and after application of the NL correction functions (note the different scale compared to the uncorrected BB SA map in Fig. 7 left), respectively. We obtain 0.2s-SAs of 1.2 to 2.0 g on the hanging-wall side in the east-central SLB. Compared to the linear BB synthetics, the NL 0.2s-SAs were reduced from >2.25g to $\sim$1.2 g in the Murray area. The largest patch of high (>1.6 g) 0.2s-SAs after application of the correction factors is located south of the Cottonwood Heights area on SRU Q02.

For scenario B' (Fig. 8 right), 0.2s-SAs are generally between 1.2 and 1.6 g in most near-fault hanging-wall areas including the central SLC area, which is a significant reduction compared to the >2.25 g from the uncorrected map (Fig. 7 right). However, there are small patches with 0.2s-SAs above 1.6 g, including one in a part of downtown SLC which is classified as Q02 in the McDonald and Ashland SRU map (Fig. 1). 0.2s-SAs also exceed 1.2 g at locations on the footwall side, which suggests that nonlinear soil behavior reduces the differences between the footwall and hanging wall side at higher frequencies.

We calculated the geometric mean of SAs, PGA and PGV from the ensemble of six scenarios after applying the site- and amplitude-dependent nonlinear corrections. Figure 9 (left) shows mean spectral accelerations at a period of 1 second. 1s-SAs exceed 0.5 g in a 5-10 km wide region on most of the hanging wall, with values of 0.75-1 g in a narrower, 3-5 km wide zone that includes downtown SLC. On the footwall side, 1s-SAs are between 0.25 and 0.75 g on the sediments in the central SLB and below 0.5 g on rock. The 1s-SAs reported by Solomon *et al.* (2004) on the hanging wall within 5–10 km of the fault trace are comparable to our values in the central and northern SLB, 0.7–1.1g, but significantly higher than our values in

the southern SLB, up to 1.3–1.5g. Perhaps more significantly, Solomon *et al.* (2004) obtained higher average 1s-SAs for the sediments on the footwall side (up to 1.1-1.5 g) than on the hanging wall side in the central SLB area - in contrast to our results (Fig. 9 left).

Our simulated mean 0.2s-SAs (Fig. 9 center) generally exceed 1 g on the hanging-wall side and on the sediments on the footwall side in the central SLB. Average PGAs from the ensemble of the six scenarios (Fig. 9 right) show a spatial distribution that is very similar to the 0.2s-SAs. PGAs average ∼0.45 g at near-fault locations on the sediments, and exceed 0.6 g in the previously identified patches on the hanging-wall side. Compared to the predicted mean 0.2s-SAs and PGAs of Solomon *et al.* (2004), our values are generally lower and show a stronger correlation with distance to the surface rupture and a weaker correlation with the SRUs.

Both 0.2s-SAs and PGAs show little contrast between the hanging-wall side and footwall side in the central SLB, where sediments are found on both sides of the fault. Average SA maps at 2s and 3s, however, show larger values on the hanging wall in most places (Roten *et al.*, 2011), including sites in the central SLB. This observation, as well as the comparison between Figures 7 and 8, suggests that soil nonlinearity helps to eliminate the differences in amplification between the deep, soft sediments on the hanging-wall side and the shallow, stiff sediments on the footwall side at higher frequencies: A low V_{S30} and deep R_1 interface, as found in SRU Q01 (Fig. 5), favor long-period amplification but also cause more high-frequency deamplification due to nonlinearity. Conversely, sites characterized by a shallow R_1 interface and higher V_{S30} (Q03) will not experience much amplification at longer periods, but are less prone to hysteretic damping at higher frequencies.

Comparison to GMPEs

We now perform a systematic comparison between the simulated 0.2s-SAs and 0.1s-SAs and the values predicted by the four GMPEs considered earlier. We calculated the different source distances and the required site characterization parameters for each SLB point on the computational grid. Source distance parameters were computed from the 3-D fault model that was used for the 3-D FD simulations. Site characterization parameters such as V_{S30}, the depth to $V_s \geq 2.5$ km·s^{-1} (required by AS08), and the depth to $Vs \geq 1.0$km·s^{-1} (required by CY08), were extracted from the WFCVM. Using these parameters, we computed spectral accelerations, PGAs and PGVs at each point on the 200 m by 200 m grid with the four GMPEs. Figure 10 shows 0.2s-SAs predicted by CB08 and AS08.

For each scenario and each location j, we evaluated the residual $r^{(j)}$ between the simulated SA ($\mathrm{SA_{sim}}$) and the value predicted by the GMPE ($\mathrm{SA_{emp}}$), and normalized it with the standard deviation of the GMPE (σ_{emp}):

$$r_j = \frac{\ln\left(\mathrm{SA}_{\mathrm{sim},j}\right) - \ln\left(\mathrm{SA}_{\mathrm{emp},j}\right)}{\sigma_{\mathrm{emp},j}}. \tag{3}$$

We binned the residuals into 50 rupture distance (R_{Rup}) categories spaced logarithmically between 1 and 22 km. We evaluated the bias by averaging over all the residuals r_k inside a distance bin:

$$B_k = \frac{1}{N_k}\sum_{1}^{N_k} r_k, \tag{4}$$

where N_k denotes the number of observations within the distance range. Thus, a positive bias indicates that the simulations overpredict the value returned by the GMPE. We evaluated the

bias for the SAs obtained from the BB synthetics on soil sites both before and after application of the nonlinear correction functions.

Figure 11 shows the bias in 0.2s-SAs and 0.1s-SAs as a function of rupture distance R_{Rup} for the GMPEs of BA08, CB08, CY08 and AS08. For 0.2s-SAs and BA08, both the linear and nonlinear biases are close to zero at rupture distances larger than 7 km. For $R_x < 5$ km, however, the bias of the linear results is close to 1 σ. After application of the nonlinear correction function, this bias is reduced to less than 0.5 σ. The same effect can be observed for the relation of CB08. This result indicates that the correction for nonlinear soil behavior makes the simulated ground motion maps more consistent with these two GMPEs.

Because CY08 and AS08 tend to predict higher ground motion values, we obtain different patterns for the bias for these two relations. At rupture distances less than 5 km, the bias is between 0 and 0.9 σ in the linear case, and between -0.25σ and -0.75σ in the nonlinear case. For rupture distances larger than 7 km, the bias is between -0.5σ and -1σ in the linear case, with larger negative values after the nonlinear correction factors are applied.

The comparison for 0.1s-SAs shows a very similar pattern. Without the nonlinear correction, the simulated values are above all the GMPEs at small rupture distances ($R_x < 5$ km), even by more than one standard deviation in the case of BA08 and CB08. The nonlinear corrections make the simulated 0.1s-SAs more consistent with the four GMPEs at $R_x < 5$ km, yielding a positive bias for BA08 and CB08, a negative bias for CY08, and a bias that averages near zero for AS08.

While the systematic comparison shows that the simulated 0.2s-SAs and 0.1s-SAs are, on average, in agreement with the four GMPEs, the spatial distribution of simulated SAs is in strong contrast with the pattern predicted by the GMPEs. Figure 10 (left) is a map of 0.2s-SAs predicted by BA08. As this relation uses only the Joyner-Boore distance to the fault, R_{JB}, areas within $R_{\mathrm{JB}} = 0$ are characterized by similar spectral accelerations regardless of the distance to the surface rupture. For example, the West Jordan area located ∼15 km from the rupture is assigned a 0.2s-SA value between 0.75 and 1.0 g by BA08. The same range of 0.2s-SAs is predicted for the area around the Holladay stepover in the immediate vicinity of the rupture. This pattern is very different from the average of the ensemble of the six simulations (Fig. 9 center), which predicts the highest ground-motion near the surface rupture on the hanging-wall side: we obtain average 0.2s-SAs above 1.25 g near the Holladay stepover, and only 0.25–0.75 g in the West Jordan area. Even though the other three GMPEs use additional source distance measurements, they share a strong dependence on R_{JB} via factors that account for higher ground motions on hanging-wall sites compared to footwall sites, see Fig. S6 of Roten *et al.* (2012). CY08 also predict similar 0.2s-SAs at near-fault locations and hanging-wall locations 15 km from the surface rupture (Fig. 10 right). Another striking difference between the mean of the ensemble (Fig. 9 center) and the relations by BA08 (Fig. 10), CY08, and AS08 is that the latter three predict higher 0.2s-SAs on the footwall-wall side than on the hanging-wall side in the central part of the SLB, see Fig. S6 of Roten *et al.* (2012). This pattern is also found in the maps by Wong *et al.* (2002b) and Solomon *et al.* (2004).

Because the amplitude of the HF component in the BB synthetics depends on the level of the LF component, maps with SAs at higher frequencies resemble those for longer periods (Fig. 9). Maps with SAs predicted by GMPEs, on the other hand, exhibit a different spatial distribution depending on the analyzed frequency, see Fig. S6 of Roten *et al.* (2012). Longer-period (2s, 3s) SAs are especially high on the hanging-wall side within ∼10 km of the surface rupture, and this pattern is also reproduced by the LF FD simulations. Shorter-period (0.1s-0.5s) SAs predicted by the GMPEs are characterized by a wider distribution of large values

extending from the western SLB well into the footwall. This behavior is not well reproduced by the BB synthetics. Possible causes for this discrepancy are discuseed in the following section.

Another observation is that the GMPEs predict lower 0.2s-SAs for sites with $V_{S30} < 300$ m·s^{-1} than for sites with higher V_{S30}, obviously by incorporating nonlinear soil effects in their site amplification terms. As a result, maps with 0.2s-SA predicted by the GMPEs feature the highest values on sediments with V_{S30} above 300 m·s^{-1} (Q02 and Q03) and $R_{\mathrm{JB}} = 0$ (compare e.g. Figs. 1 and 10). The wedge-shaped region extending from downtown Salt Lake City to Murray is classified as Q01 (Fig. 1) and characterized by $V_{S30} < 300$ m·s^{-1} (Fig. 5 top), which is expressed in the generally low 0.2s-SAs that BA08 and CB08 predict for this area. Our simulated BB synthetics corrected for nonlinear soil behavior, on the other hand, do not show this drastic deamplification for 0.2s-SAs at Q01 sites. However, nonlinear soil effects reduce the difference between sites located on Q01 and Q02. The reason for the lack of deamplification on Q01 could be the rather high reference strain that we assigned to sites belonging to Q01, which reflects the high clay component of the Bonneville soils and the results of laboratory tests on soil samples (Bay and Sasanakul, 2005). The GMPEs, on the other hand, are only estimating soil nonlinearity as a function of the V_{S30}, without taking into account specific soil types.

Uncertainty of computed NL BB ground motions for the SLV

In this section we discuss the limitations and major sources of uncertainty for our M 7 scenario earthquake ground motions in the SLV.

Computation of (linear) BB ground motions

Published hybrid BB generation methods differ in the details of merging the LF and HF portions of the synthetics, as well as in the dependency of the HF part on the local impedance structure. For example, the method by Graves and Pitarka (2010) incorporates effects of the velocity structure into the HF part of the spectrum, which is otherwise independent of the LF spectral level. On the other hand, the HF scatterograms computed by the method of Mai *et al.* (2010) are scaled with the amplitude of the LF spectra at the matching frequency (0.9±0.1 Hz), in part to minimize numerical artifacts at the merging frequency for the LF and HF portions, but also to transfer impedance effects from the LFs into the HFs. This dependency between the amplitude of the LF and HF components in the BB synthetics causes, to some extent, the distributions of SAs at higher frequencies to resemble those for longer periods (Fig. 9). Maps with SAs predicted by GMPEs generally exhibit a different spatial distribution depending on the analyzed frequency, as noted in the previous section, see Fig. S6 of Roten *et al.* (2012). Future validation exercises for normal-faulting events should focus on resolving this issue.

Computation of nonlinear ground motions

The assumptions involved in simulating nonlinear soil behavior represent some limitations to this study. A first source of uncertainty concerns the nonlinear soil parameters γ_r and $\xi_{\max}$. While the empirical relations we used to estimate these parameters were modified based on laboratory tests of Bonneville clay samples, only one of the sampling locations was inside the area considered for this study. No laboratory measurements were performed on soil

samples representing SRU Q02 and Q03, so the lower reference strain assigned to these units is based solely on the relationship by Darendeli (2001). To analyze the sensitivity of our results to parameter selection we included soil models that represent 1σ limits of soil nonlinearity. Results obtained with the lower bound nonlinear model (Fig. 3) suggest that nonlinearity has a significant impact at near-fault hanging-wall sites even for a more conservative choice of reference strain. Furthermore, we have demonstrated that the degree of nonlinear damping is also largely controlled by V_{S30} and the depth to the R_1 interface, which are reasonably well-constrained parameters (Magistrale *et al.*, 2008).

The simplicity of the soil model, which neglects dilatancy, constitutes a further limitation. Observations of spiky waveforms, e.g. during the 1987 Superstition Hills (Holzer *et al.*, 1989; Zeghal and Elgamal, 1994), the 1995 Hyoge-ken Nanbu (Kamae *et al.*, 1998) and the 1993 Kushiro-Oki earthquake (Iai *et al.*, 1995) support the idea that soft soils partly recover their shear strength under cyclic loads due to their dilatant nature (Bonilla *et al.*, 2005). During this short recovery phase the soil regains its capability to transmit the incoming seismic energy to the surface, leading to characteristic cusped waveforms that represent large amplifications. Modeling dilatancy with NOAH requires 5 additional parameters, which need to be calibrated from stress-controlled laboratory experiments (e.g. Iai *et al.*, 1990; Bonilla, 2001; Roten *et al.*, 2009). To our knowledge, no such measurements have been performed on soil samples from the Salt Lake region, which led us to ignore dilatancy in our nonlinear simulations. Including dilatancy may result in higher spectral accelerations especially on the hanging-wall side.

An additional uncertainty arises from correcting the SAs for nonlinearity with the empirically-derived correction functions, as the relations between linear and nonlinear SAs show a lot of variability. Calculating the 1-D nonlinear site response for each location on the computational grid individually would eliminate the need for this approximation. This goal could be achieved by performance optimizations in NOAH and by embedding the code into a parallel program that runs on 100s of CPU cores, which would allow the computation of the 1-D nonlinear response for the whole SLB within a practical time frame.

Finally, the assumption that the site response is adequately represented by a 1-D model is likely to represent the largest limitation. In geotechnical engineering it is generally accepted that the major part of ground shaking is related to upward propagation of body waves (e.g. Ishihara, 1996). This assumption is often justified with the bending of seismic rays towards the Earth's surface, since seismic velocities increase with depth in a typical geological setting. However, Bard and Bouchon demonstrated in 1980 that Love waves generated at a basin edge may have much larger amplitudes than the direct incident signal even in the case of vertical incidence. Such basin-diffracted waves have been identified in many weak motion records (e.g. Field, 1996; Hartzell *et al.*, 2003; Roten *et al.*, 2008). The physics of surface wave propagation in nonlinear media is an ongoing field of research, and numerical codes are under development that will allow the treatment of wave propagation in nonlinear materials in two (e.g. Bonilla *et al.*, 2006) or three dimensions (e.g. Taborda and Bielak, 2008) in the future.

Conclusions

We establish amplitude-dependent relations betweens SAs derived from BB synthetics and SAs resulting from the fully nonlinear 1-D simulations in the SLB for M 7.0 earthquake scenarios on the WFSLC. Coefficients for these relations are calibrated for each considered frequency and each of the three site response units. We apply these relations to correct our BB SA maps for nonlinear soil behavior. We find that, after taking soil nonlinearity into account, the largest 1s-SAs still occur on the hanging wall side of the fault, where they exceed 0.75

g. 0.2s-SAs are generally above 1 g within a few km of the fault on the hanging-wall and on the footwall sediments in the central SLB. In a few isolated areas, 0.2s-SAs exceed 1.25 g, especially on Q02 in the southern part of the SLB. Near-fault PGAs range from 0.45 to >0.6g.

Compared to ground motion maps generated in previous studies (Wong *et al.*, 2002b; Solomon *et al.*, 2004), our ground motion values are lower and have a different spatial pattern. The differences between our ground motion results and those obtained by Wong *et al.* (2002b) and Solomon *et al.* (2004) are likely caused by differences in the simulation methods. 0.2s-SAs and 0.1s-SAs corrected for nonlinear soil behavior compare favorably with values predicted by four GMPEs, including areas at close distances (< 5 km) from the rupture. However, on our maps the ground motions decrease more rapidly with distance from the surface rupture.

Further comparisons against strong motion data are required to validate the simulated ground motions in the future.

Data and resources

The Wasatch Front Community Velocity Model (WFCVM) is available from the Utah Geological Survey (`http://geology.utah.gov/ghp/consultants/geophysical_data/cvm.htm`). The nonlinear 1-D code NOAH (Bonilla *et al.*, 2005) and the BB toolbox (Mai *et al.*, 2010; Mena *et al.*, 2010) are available from their authors upon request. Maps presented in this text were made using the Generic Mapping Tools version 4.5.0 (`http://www.soest. hawaii.edu/gmt`) by Wessel and Smith (1998). 2-D plots were created with the Matplotlib graphics package (`http://matplotlib.sourceforge.net`) for Python (Hunter, 2007). We used the OPENSHA attenuation relationship plotter (`http://www.opensha.org`) and the MatLab™scripts from the Baker research group (`http://www.stanford.edu/~bakerjw/attenuation.html`) to generate attenuation curves.

Tables

Table 1: Site response units, Plasticity Index (PI') and average V_{S30}.

Unit(s)	Description (McDonald and Ashland, 2008)	PI'	$\overline{V_{S30}}$ ($m \cdot s^{-1}$)
Q01	Lacustrine and alluvial silt, clay and fine sand; alluvial, lateral-spread, or marsh deposits typically overlie lacustrine deposits	40%	250
Q02	Lacustrine sand and gravel; interbedded lacustrine silt, clay and sand; latest Pleistocene to Holocene alluvial fan deposits	30%	375
Q03	Lacustrine and alluvial gravel and sand; pre-Bonneville alluvial fan deposits, primarily where they occur on the footwall of the Wasatch fault	0%	507
T,M,P	Tertiary, mesozoic, paleozoic or precambrian rock; treated as linear.		

Acknowledgements

This research was supported by the U.S. Geological Survey, Department of the Interior, under USGS award number G11AP20055. The views and conclusions contained in this document are those of the authors and should not be interpreted as necessarily representing the official policies, either expressed or implied, of the U.S. Government.

References

Abrahamson, N., and Silva, W. 2008. Summary of the Abrahamson & Silva NGA ground-motion relations. *Earthquake Spectra*, **24**(1), 67–97.

Bard, P.-Y., and Bouchon, M. 1980. The seismic response of sediment-filled valleys. Part 1. The case of incident SH waves. *Bull. seism. Soc. Am.*, **70**(4), 1263–1286.

Bay, J.A., and Sasanakul, I. 2005. *Measurement of nonlinear dynamic properties of Bonneville silty-clays.* Award 04HQGR0055. Utah State Univ., Department of Civil and Environmental Engineering.

Black, B.D., Lund, W.R., and Mayes, B.H. 1995. Large earthquakes on the Salt Lake City segment of the Wasatch fault zone-summary of new information from the South Fork Dry Creek site, Salt Lake County, Utah. *Pages 11–30 of: Environmental and Engineering Geology of the Wasatch Front Region: 1995 Symposium and Field Conference. W.R. Lund(Editor).* Utah Geological Association Publication 24.

Bonilla, LF. 2001. NOAH: Users Manual. *Institute for Crustal Studies, University of California, Santa Barbara.*

Bonilla, L.F., Archuleta, R.J., and Lavallee, D. 2005. Hysteretic and Dilatant Behavior of Cohesionless Soils and Their Effects on Nonlinear Site Response: Field Data Observations and Modeling. *Bull. Seism. Soc. Am.*, **95**(6), 2373–2395.

Bonilla, L.F., Luis, P.-C., and Nielsen, S. 2006. 1D and 2D linear and nonlinear site response in the Grenoble area. *In: Third International Symposium on the Effects of Surface Geology on Seismic Motion, Grenoble, France, 30 August - 1 September 2006.*

Boore, D. M., and Atkinson, G. M. 2008. Ground-Motion Prediction Equations for the Average Horizontal Component of PGA, PGV, and 5%-Damped PSA at Spectral Periods between 0.01 s and 10.0 s. *Earthquake Spectra*, **24**(1), 99–138.

Borcherdt, R.D. 1994. Estimates of site-dependent response spectra for design (methodology and justification). *Earthq. Spectra*, **10**, 617653.

Campbell, K. W., and Bozorgnia, Y. 2008. NGA Ground Motion Model for the Geometric Mean Horizontal Component of PGA, PGV, PGD and 5% Damped Linear Elastic Response Spectra for Periods Ranging from 0.01 to 10 s. *Earthquake Spectra*, **24**(1), 139–171.

Chiou, B., Darragh, R., Gregor, N., and Silva, W. 2008. NGA strong-motion database. *Earthquake Spectra*, **24**(1), 23–44.

Chiou, B.S.J., and Youngs, R.R. 2008. An NGA model for the average horizontal component of peak ground motion and response spectra. *Earthquake Spectra*, **24**(1), 173–215.

Cui, Y., Olsen, K.B., Lee, K., Zhou, J., Small, P., Roten, D., Ely, G., Panda, D.K., Chourasia, A, Levesque, J., Day, S.M., and Maechling, P. 2010. Scalable Earthquake Simulation on Petascale Supercomputers. *In: Proceedings of SC10, November 13-19, New Orleans, LA.*

Darendeli, Mehmet B. 2001. *Development of a new family of normalized modulus reduction and material damping curves.* Ph.D. thesis, The University of Texas at Austin.

Field, E. H. 1996. Spectral amplification in a sediment-filled valley exhibiting clear basin-edge-induced waves. *Bull. seism. Soc. Am.*, **86**, 991–1005.

Graves, R.W., and Pitarka, A. 2010. Broadband Ground-Motion Simulation Using a Hybrid Approach. *Bull. seism. Soc. Am.*, **100**(5A), 2095.

Hartzell, S., Carver, D., Williams, R. A., Harmsen, S., and Zerva, A. 2003. Site Response, Shallow Shear-Wave Velocity, and Wave Propagation at the San Jose, California, Dense Seismic Array. *Bull. seism. Soc. Am.*, **93**(1), 443–464.

Hartzell, S., Bonilla, L. F., and Williams, R.A. 2004. Prediction of Nonlinear Soil Effects. *Bull. Seism. Soc. Am.*, **94**(5), 1609–1629.

Hartzell, S., Guatteri, M., Mai, P.M., Liu, P.-C., and Fisk, M. 2005. Calculation of Broadband Time Histories of Ground Motion, Part II: Kinematic and Dynamic Modeling Using Theoretical Green's Functions and Comparison with the 1994 Northridge Earthquake. *Bull. seism. Soc. Am.*, **95**(2), 614–645.

Hill, J., Benz, H., Murphy, M., and Schuster, G. 1990. Propagation and resonance of SH waves in the Salt Lake Valley, Utah. *Bull. Seism. Soc. Am.*, **80**(1), 23–42.

Holzer, T.L., Youd, T. L., and Hanks, T.C. 1989. Dynamics of Liquefaction during the 1987 Superstition Hills, California, Earthquake. *Science*, **244**(4900), 56–59.

Hunter, John D. 2007. Matplotlib: A 2D Graphics Environment. *Computing in Science and Engineering*, **9**, 90–95.

Iai, S., Matsunaga, Y., and Kameoka, T. 1990. Parameter identification for a cyclic mobility model. *Report of the Port and Harbour Research Institute*, **29**, 57–83.

Iai, S., Morita, T., Kameoka, T., Matsunaga, Y., and Abiko, K. 1995. Response of a dense sand deposit during 1993 Kushiro-Oki Earthquake. *Soils Found.*, **35**, 115–131.

Ishihara, K. 1996. *Soil Behaviour in Earthquake Geotechnics.* Clarenton Press, Oxford.

Kamae, K., Irikura, K., and Pitarka, A. 1998. A technique for simulating strong ground motion using hybrid Green's function. *Bull. seism. Soc. Am.*, **88**(2), 357.

Konno, K., and Ohmachi, T. 1998. Ground-Motion Characteristics Estimated from Spectral Ratio between Horizontal and Vertical Components of Microtremor. *Bull. seism. Soc. Am.*, **88**(1), 228–241.

Magistrale, H., Olsen, K., and Pechmann, J. 2008. *Construction and Verification of a Wasatch Front Community Velocity Model: Collaborative Research with San Diego State University and the University of Utah.* Final Technical Report submitted to NEHRP. U.S. Geological Survey.

Mai, P. M., Imperatori, W., and Olsen, K. B. 2010. Hybrid Broadband Ground-Motion Simulations: Combining Long-Period Deterministic Synthetics with High-Frequency Multiple S-to-S Backscattering. *Bull. seism. Soc. Am.*, **100**(5A), 2124–2142.

Mai, P.M., and Beroza, G.C. 2003. A hybrid method for calculating near-source, broadband seismograms: application to strong motion prediction. *Phys. Earth Planet. Int.*, **137**, 183–199.

McCalpin, J., and Nelson, C. 2000. *Long recurrence records from the Wasatch fault zone.* Final technical report. U.S. Geological Survey, National Earthquake Hazards Reduction Program, Contract number 99HQGR0058.

McCalpin, J.P., and Nishenko, S.P. 1996. Holocene paleoseismicity, temporal clustering, and probabilities of future large (M>7) earthquakes on the Wasatch fault zone, Utah. *J. Geophys. Res.*, **101**, 6233–6253.

McDonald, G.N., and Ashland, F.X. 2008. *Earthquake site conditions in the Wasatch Front urban corridor, Utah.* Special Study 125. Utah Geol. Surv.

Mena, B., Durukal, E., and Erdik, M. 2006. Effectiveness of Hybrid Green's Function Method in the Simulation of Near-Field Strong Motion: An Application to the 2004 Parkfield Earthquake. *Bull. seism. Soc. Am.*, **96**(4B), S183–205.

Mena, B., Mai, P. M., Olsen, K. B., Purvance, M. D., and Brune, J. N. 2010. Hybrid Broadband Ground-Motion Simulation Using Scattering Green's Functions: Application to Large-Magnitude Events. *Bull. seism. Soc. Am.*, **100**(5A), 2143–2162.

O'Connell, D. R. H., Ma, S., and Archuleta, R. J. 2007. Influence of Dip and Velocity Heterogeneity on Reverse- and Normal-Faulting Rupture Dynamics and Near-Fault Ground Motions. *Bull. seism. Soc. Am.*, **97**(6), 1970–1989.

Olsen, K., and Pechmann, J. 20011. *Final Technical Report for USGS Awards 06HQGR0205 and 06HQGR0206.* Final Technical Report submitted to NEHRP. U.S. Geological Survey.

Olsen, K. B., Day, S. M., Dalguer, L. A., Mayhew, J., Cui, Y., Zhu, J., Cruz-Atienza, V., Roten, D., Maechling, P., Jordan, T., Okaya, D., and Chourasia, A. 2009. ShakeOut-D: Ground Motion Estimates Using an Ensemble of Large Earthquakes on the Southern San Andreas Fault With Spontaneous Rupture Propagation. *Geophys. Res. Lett.*, **36**, L04303.

Pitarka, A., Somerville, P., Fukushima, Y., Uetake, T., and Irikura, K. 2000. Simulation of Near-Fault Strong-Ground Motion Using Hybrid Green's Functions. *Bull. seism. Soc. Am.*, **90**(3), 566–586.

Roten, D., Fäh, D., Olsen, K.B., and Giardini, D. 2008. A comparison of observed and simulated site response in the Rhône valley. *Geophys. J. Int.*, **173**(June), 958–978.

Roten, D., Fäh, D., Bonilla, LF, Alvarez-Rubio, S., Weber, TM, and Laue, J. 2009. Estimation of non-linear site response in a deep Alpine valley. *Geophys. J. Int.*, **178**(3), 1597–1613.

Roten, D., Olsen, K. B., Pechmann, J., Cruz-Atienza, V., and Magistrale, H. 2011. 3-D Simulations of M 7 Earthquakes on the Wasatch fault, Utah, Part I: Long-period (0-1 Hz) ground motions. *Bull. seism. Soc. Am.*, **101**(5), 2045–2063.

Roten, D., Olsen, K.B., and Pechmann, J. 2012. 3-D Simulations of M7 Earthquakes on the Wasatch fault, Utah, Part II: Broadband (0-10 Hz) Ground Motions and Nonlinear Soil Behavior. *Bull. Seis. Soc. Am.*, **102**, 2008–2030.

Schnabel, P., Seed, H. Bolton, and Lysmer, J. 1972. Modification of seismograph records for effects of local soil conditions. *Bull. Seism. Soc. Am.*, **62**(6), 1649–1664.

Silva, W.J., Wong, I.G., and Darragh, R.B. 1998. Engineering characterization of earthquake strong ground motions in the Pacific Northwest. *Pages 313–324 of:* Rogers, A.M., Walsh, T.J., Kockleman, W.J., and Priest, G.R. (eds), *Assessing Earthquake Hazards and Reducing Risk in the Pacific Northwest*, vol. 2. U.S. Geological Survey Professional Paper 1560.

Solomon, B.J., Storey, N., Wong, I., Gregor, N., Wright, D., and McDonald, G. 2004. *Earthquake-hazards scenario for a M7 earthquake on the Salt Lake City segment of the Wasatch fault zone, Utah.* Utah Geol. Surv. Spec. Study 111DM, CD-ROM, 59pp., 6pl.

Taborda, R., and Bielak, J. 2008. *Three-dimensional modeling of earthquake ground motion in basins, including nonlinear wave propagation in soils.* Final Technical Report, USGS Award 08HQGR0018.

Vucetic, M., and Dobry, R. 1991. Effect of soil plasticity on cyclic response. *J. Geotech. Eng.*, **117**(1), 89–107.

Wessel, P., and Smith, W.H.F. 1998. New, improved version of Generic Mapping Tools released. *EOS Trans. AGU*, **79**(47), 579.

Wong, I., Silva, W., Olig, S, Thomas, P., Wright, D., Ashland, N., Gregor, N., Pechmann, M., Dober, M., Christenson, G., and Gerth, R. 2002a. *Earthquake scenario and probabilistic ground shaking maps for the Salt Lake City, Utah, metropolitan area.* Misc. Pub. MP-02-5. Utah Geol. Surv.

Wong, I., Silva, W., Gregor, N., Wright, D., Ashland, F., McDonald, G., Olig, S., Christenson, G., and Solomon, B. 2002b. Earthquake scenario ground shaking maps for the central Wasatch Front, Utah. *In: Proceedings of the 7th U.S. National Conference on Earthquake Engineering, Boston, Mass., July 21-25, 2002.*

Zeghal, M., and Elgamal, A.W. 1994. Analysis of site liquefaction using earthquake records. *Journal of Geotechnical Engineering;(United States)*, **120**(6).

Zeng, Y., Anderson, J. G., and Feng, S. 1995. Subevent rake and random scattering effects in realistic ground motion simulation. *Geophys. Res. Lett.*, **22**(1), 17–20.

Figure 1: Map of the Salt Lake basin showing the distribution of site response units inside the computational area and the location of the three cross-sections used for nonlinear simulations. The thick white line along the Wasatch Front represents the surface rupture of the WFSLC. Green letters represent the epicenter locations in the six rupture models. Modified from McDonald and Ashland (2008).

Figure 2: *Top panels:* 0.2s-SAs predicted by four NGA equations and computed from linear BB synthetics along profile P0 for source model B *(top left)* and along profile P1 for source model B' *(top right)*. See Figure 1 for profile locations. The thin black lines show the largest median plus one standard deviation and the smallest median minus one standard deviation of all four considered NGA Models. *Bottom panels*: Cross-sections through the WFCVM showing the shear-wave velocity. The black lines indicate the fault.

Figure 3: Same as Figure 2, but showing SAs derived from fully nonlinear 1-D simulations. The hatched areas depict SAs obtained from the upper- and lower-bound nonlinear models, using $(\gamma_r - \sigma,\ \xi_{\max} + \sigma_r)$ and $(\gamma_r + \sigma,\ \xi_{\max} - \sigma_r)$, respectively.

Figure 4: 0.2s-SAs obtained from nonlinear simulations as a function of corresponding linear values for site response units Q01 *(A)*, Q02 *(B)* and Q03 *(C)*. Solid lines depict the amplitude- and site-dependent correction functions, obtained by fitting a third-order polynomial through these data. Dashed lines depict the correction functions derived from nonlinear simulations with the upper- and lower-bound soil models. (Individual data points are shown for the mean soil model only.)

Figure 5: Distribution of average shear-wave velocity in the top 30 meters V_{S30} *(A)* and depth to the R_1 interface *(B)* on the three SRUs. Counts were normalized to form a probability density function.

Figure 6: Typical shear stress-strain relationship of soil under cyclic loads for a hyperbolic model. Backbone and reloading curves were computed using a reference strain γ_r of 0.1% and two different values for the shear modulus G_0, corresponding to shear-wave velocities of 250 and 300 m·s^{-1} and a density of 2000 kgm^{-3}. The pair (γ_t, τ_t) represents the point where the path reverses from loading to unloading. Modified from Bonilla (2001).

Figure 7: Maps of orientation-independent spectral accelerations obtained from linear BBs based on rupture model B *(left panel)* and from rupture model B' *(right panel)* at 5 Hz. Yellow stars depict the hypocenters. The gray lines depict the WF (thick) and major roads and freeways (thin).

Figure 8: Maps of orientation-independent spectral accelerations, corrected for nonlinear soil behavior. *Left panel:* 0.2s-SAs for rupture model B. *Right panel:* 0.2s-SAs for rupture model B'.

Figure 9: Average 1s-SAs (left), 0.2s-SAs (center) and PGAs (right) from the six scenarios after application of nonlinear correction functions.

Figure 10: 0.2s-SAs predicted by the GMPE of BA08 *(left)* and CY08 *(right)*.

Figure 11: Bias of simulated 0.2s-SAs and 0.1s-SAs on SLB sediments compared to four GMPEs (eq. 4). Shaded areas show standard deviations of the residuals from our linear results; errorbars show standard deviations of the nonlinear residuals.

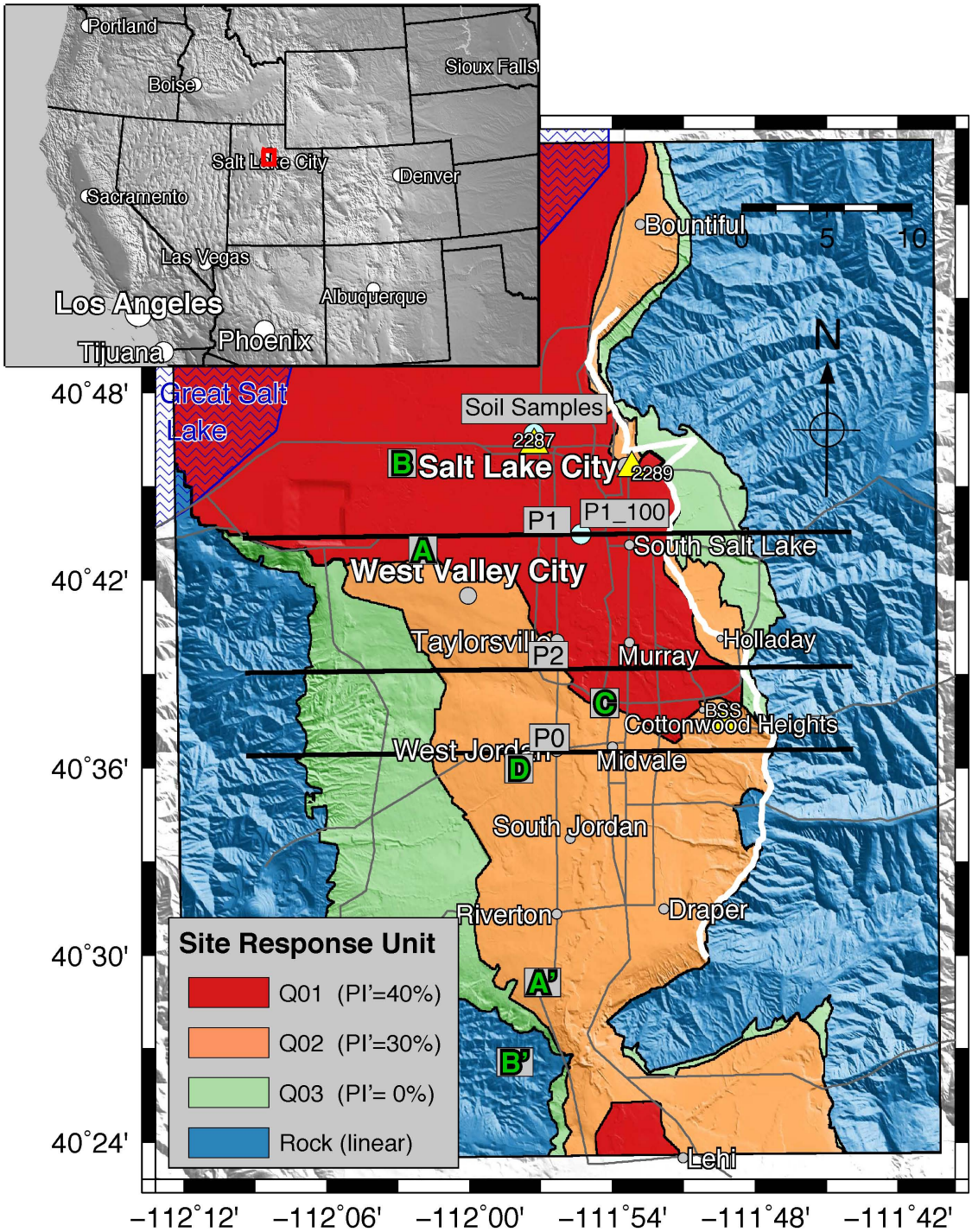
Portland
Boise
Sioux Falls
Salt Lake City
Denver
Sacramento
Las Vegas
Los Angeles
Albuquerque
Phoenix
Tijuana
Great Salt Lake
Soil Samples
2287
2289
B Salt Lake City
P1
P1_100
A
West Valley City
South Salt Lake
Bountiful
Taylorsville
P2
Murray
Holladay
C
BSS
Cottonwood Heights
P0
West Jordan
D
Midvale
South Jordan
Riverton
Draper
A'
B'
Lehi
0
5
10
N
40˚48'
40˚42'
40˚36'
40˚30'
40˚24'
−112˚12'
−112˚06'
−112˚00'
−111˚54'
−111˚48'
−111˚42'
Site Response Unit
Q01 (PI'=40%)
Q02 (PI'=30%)
Q03 (PI'= 0%)
Rock (linear)

Figure 1:

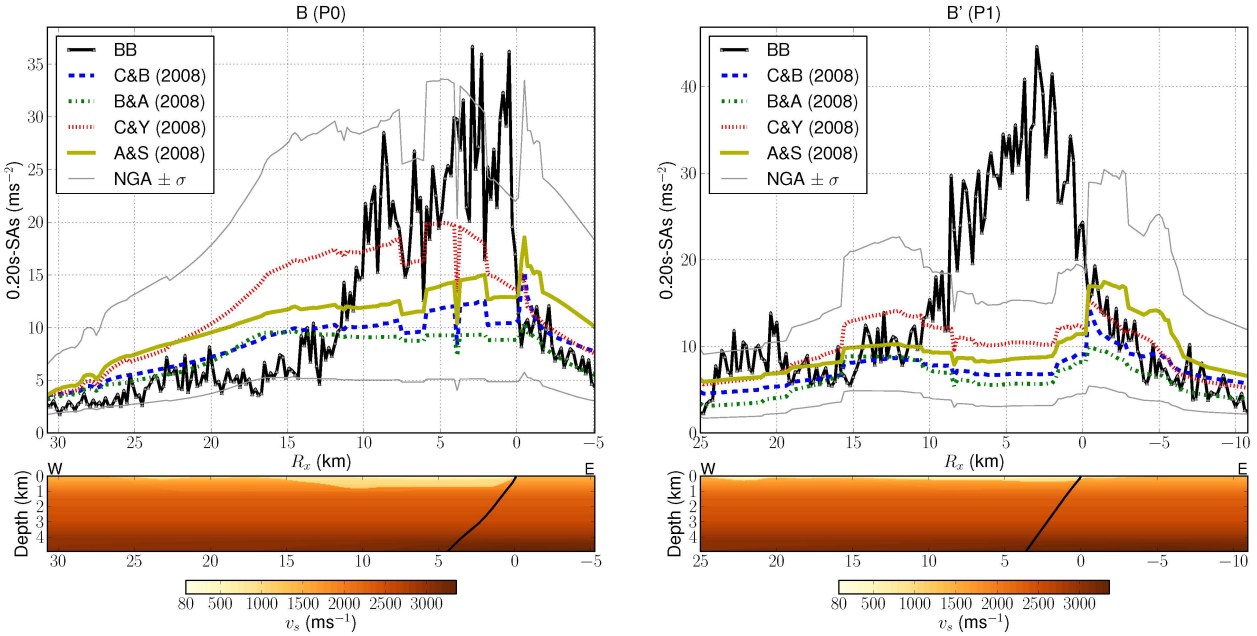

Figure 2:

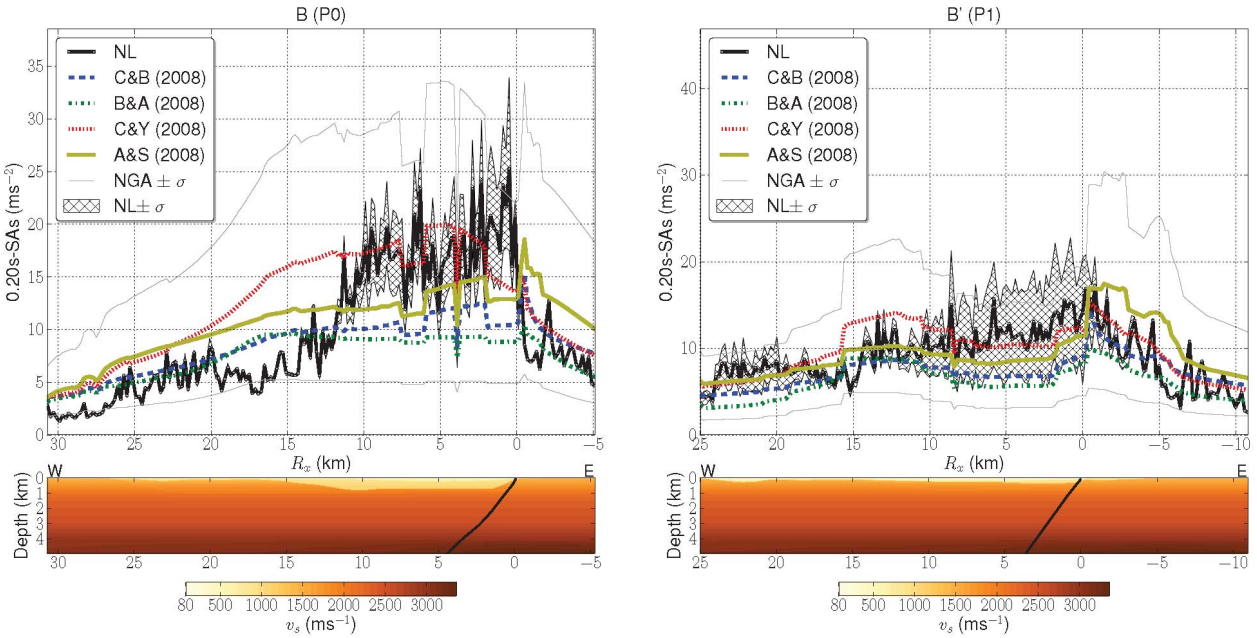

Figure 3:

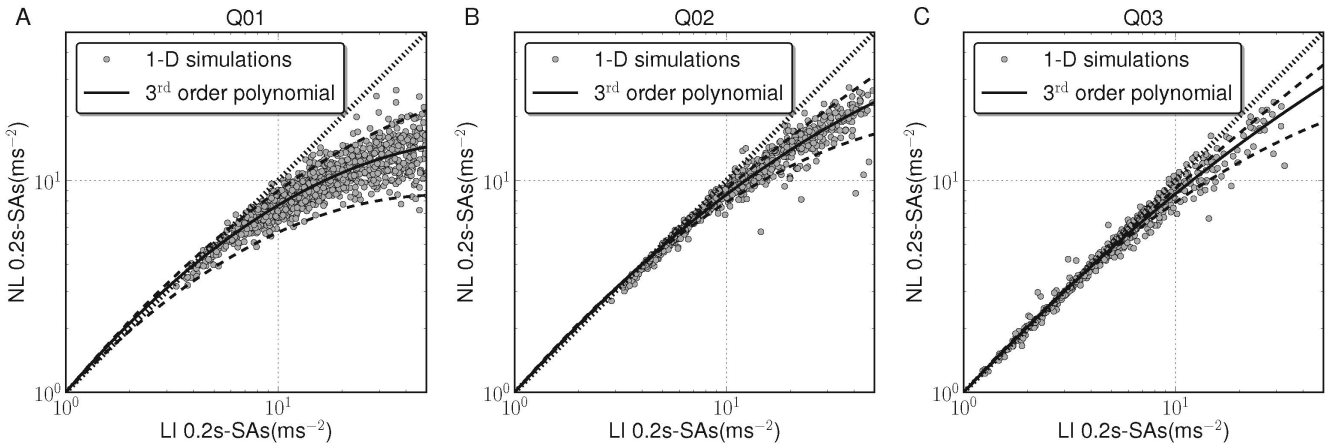

Figure 4:

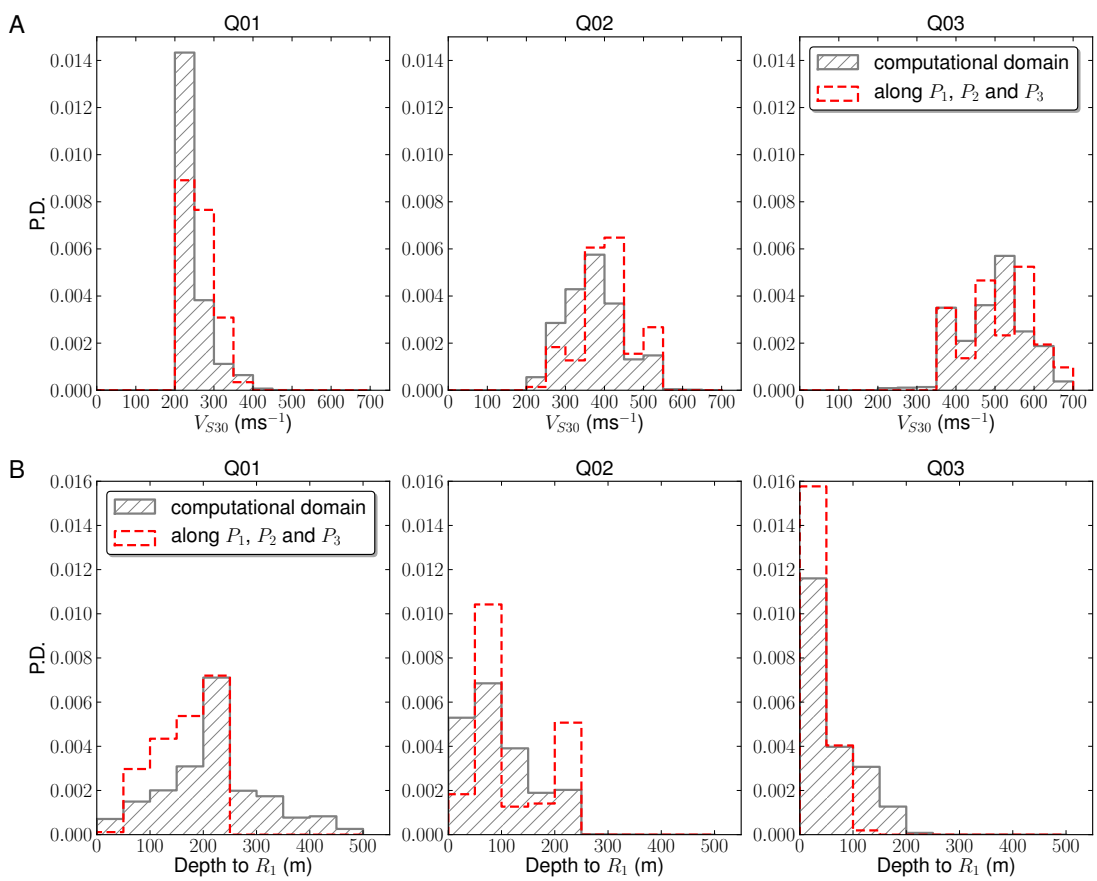

Figure 5:

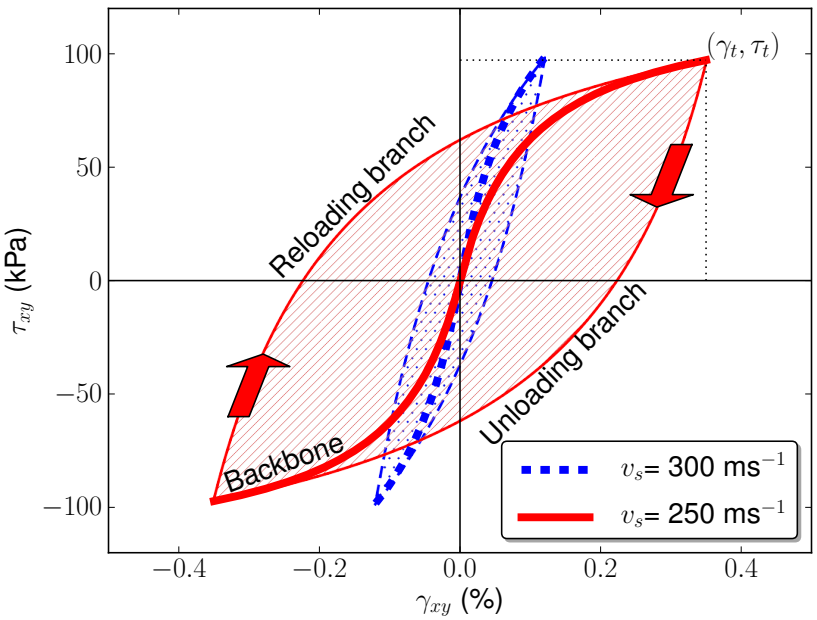

Figure 6:

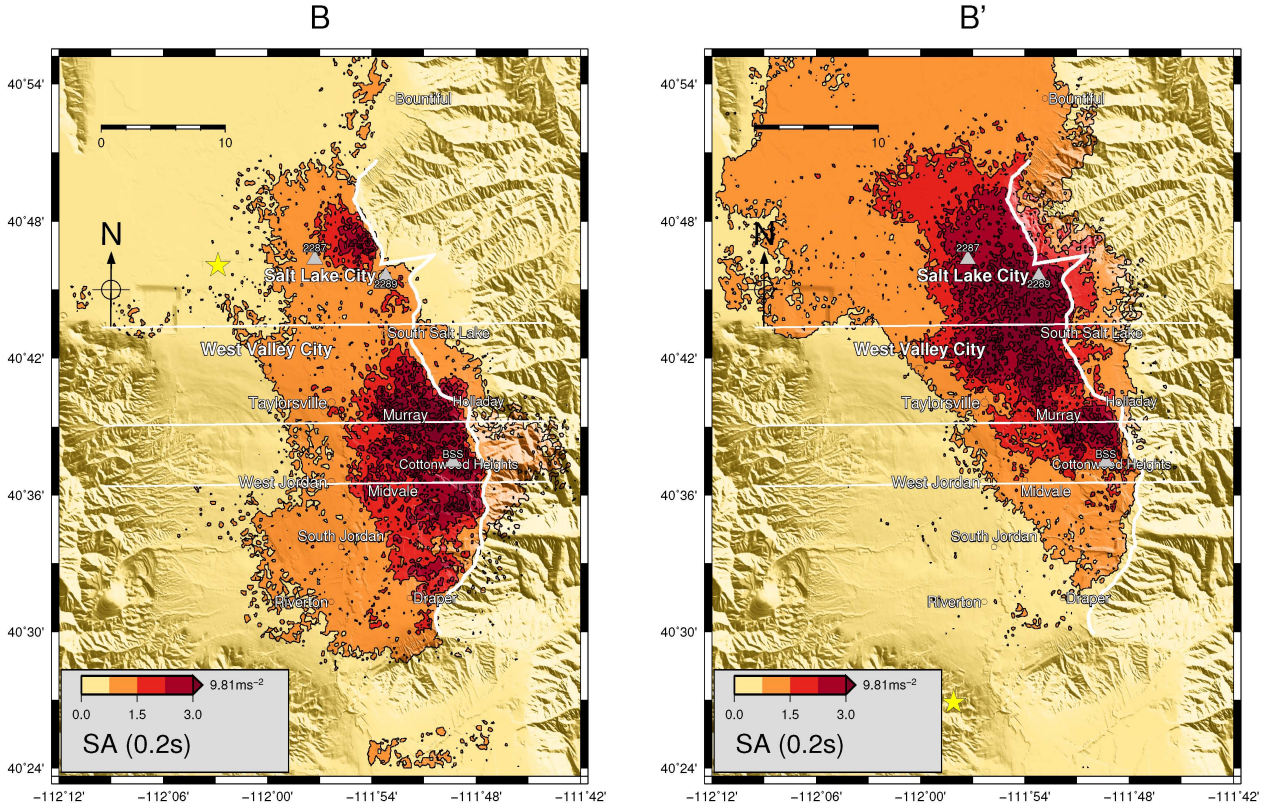

Figure 7:

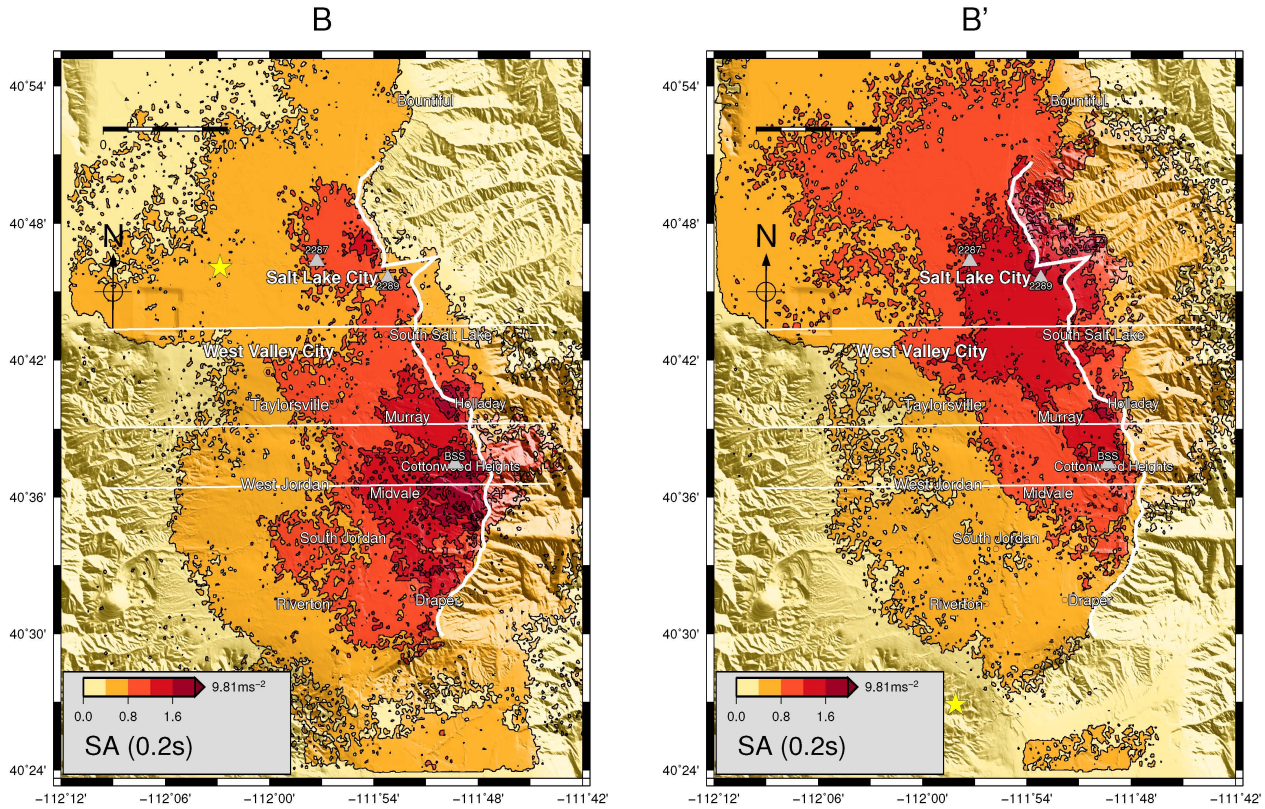
B
B'
Bountiful
Salt Lake City
South Salt Lake
West Valley City
Taylorsville
Murray
Holladay
Cottonwood Heights
West Jordan
Midvale
South Jordan
Riverton
Draper
N
9.81ms^{-2}
0.0
0.8
1.6
SA (0.2s)
40°54'
40°48'
40°42'
40°36'
40°30'
40°24'
−112°12'
−112°06'
−112°00'
−111°54'
−111°48'
−111°42'

Figure 8:

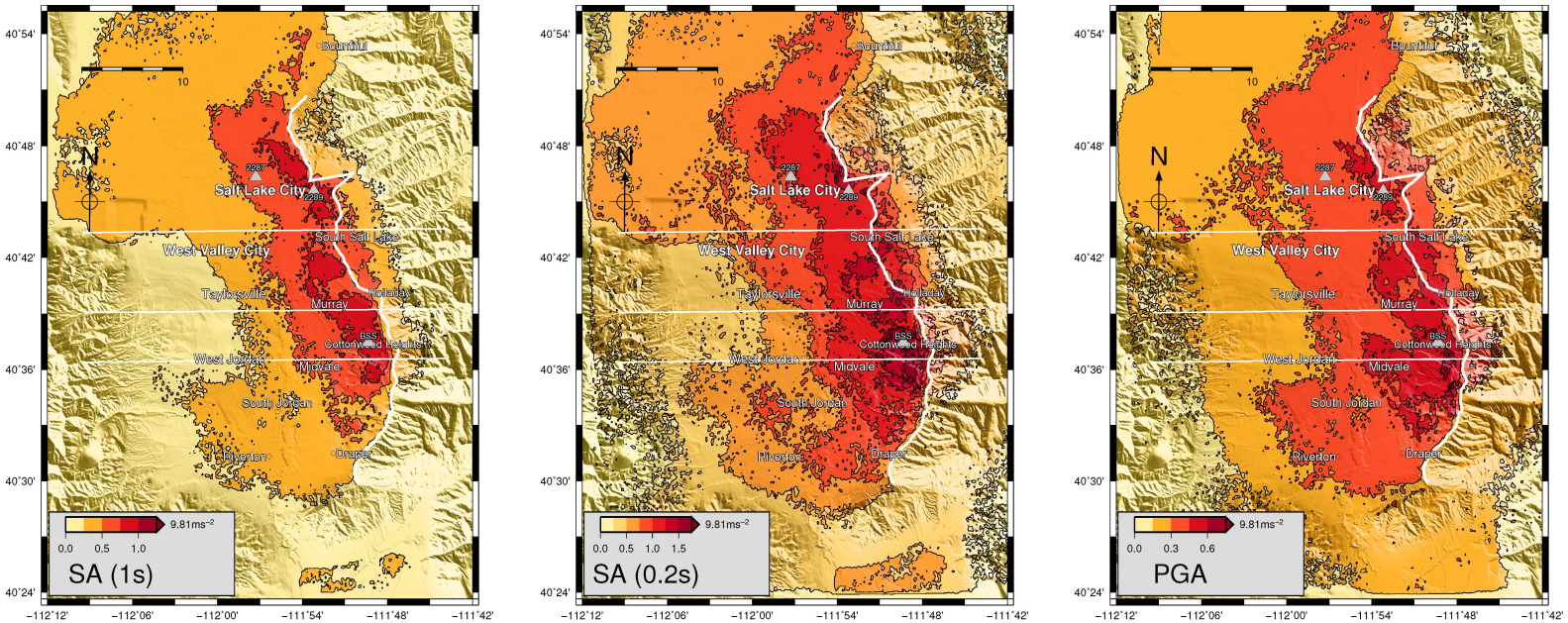
SA (1s)
SA (0.2s)
PGA
9.81ms^{-2}
N
10
Salt Lake City
West Valley City
South Salt Lake
Taylorsville
Murray
Holladay
West Jordan
Midvale
South Jordan
Riverton
Draper
Bountiful
Cottonwood Heights
40°54'
40°48'
40°42'
40°36'
40°30'
40°24'
−112°12'
−112°06'
−112°00'
−111°54'
−111°48'
−111°42'

Figure 9:

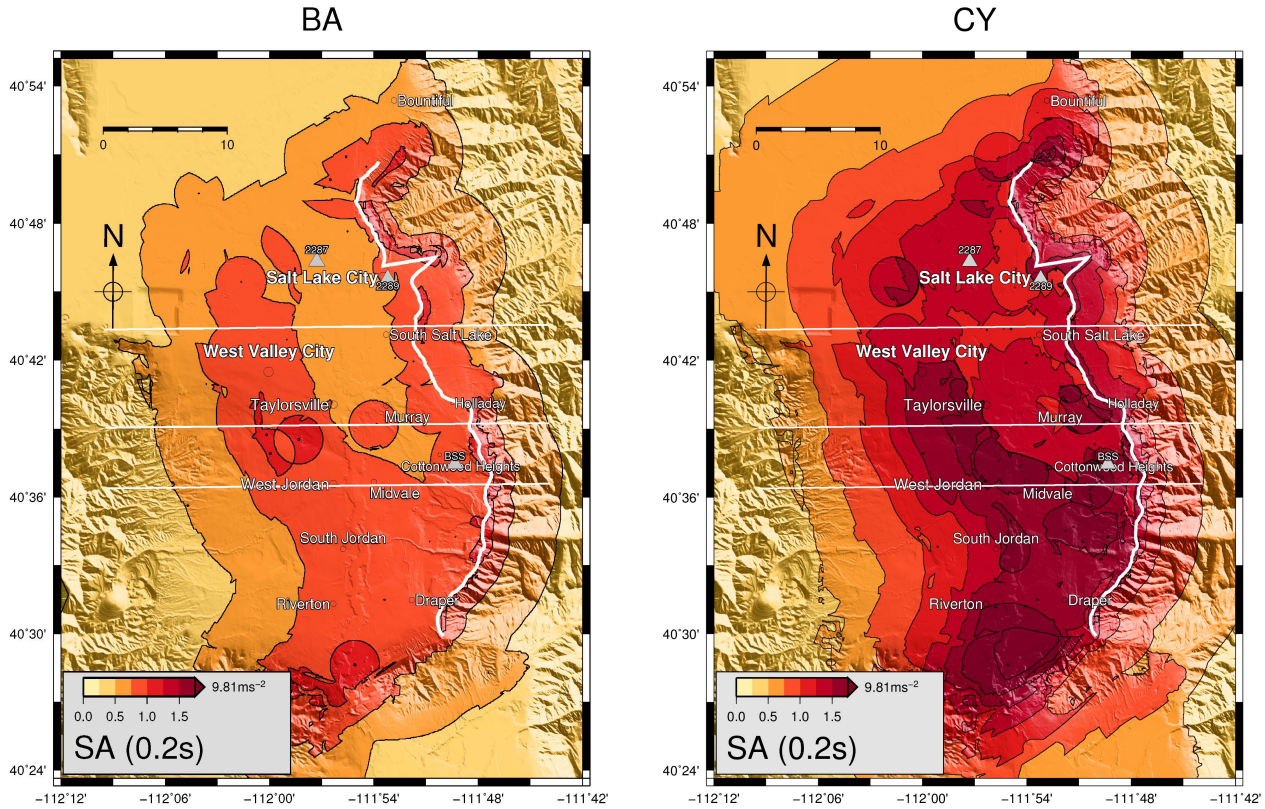
BA
CY
N
0
10
Bountiful
Salt Lake City
2287
2289
South Salt Lake
West Valley City
Taylorsville
Murray
Holladay
BSS
Cottonwood Heights
West Jordan
Midvale
South Jordan
Riverton
Draper
9.81ms^{-2}
0.0 0.5 1.0 1.5
SA (0.2s)
40°54'
40°48'
40°42'
40°36'
40°30'
40°24'
−112°12'
−112°06'
−112°00'
−111°54'
−111°48'
−111°42'

Figure 10:

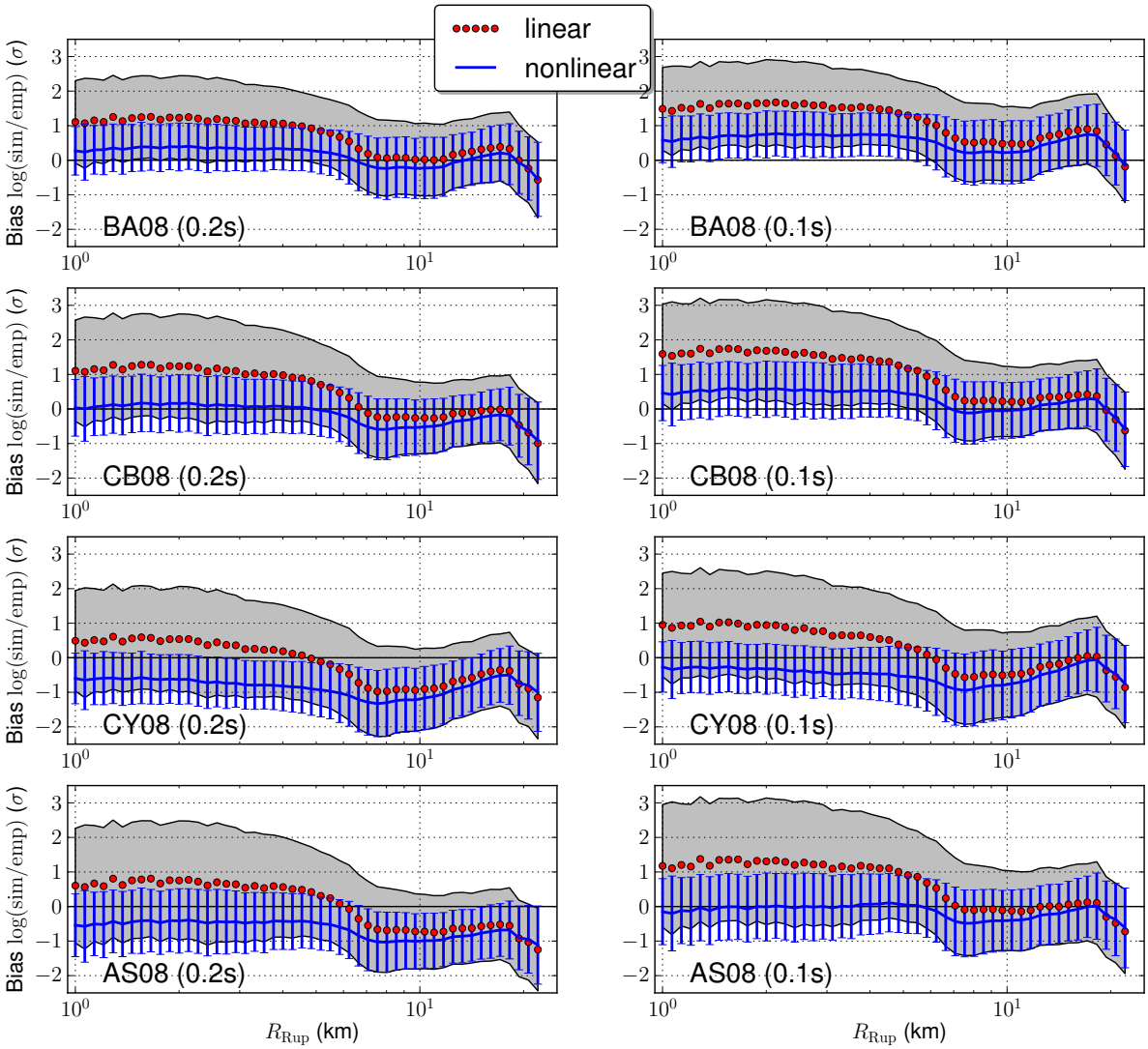
linear
nonlinear
Bias log(sim/emp) (σ)
BA08 (0.2s)
BA08 (0.1s)
CB08 (0.2s)
CB08 (0.1s)
CY08 (0.2s)
CY08 (0.1s)
AS08 (0.2s)
AS08 (0.1s)
R_{Rup} (km)

Figure 11: